



Article

Interfacial Modification of Mesoporous TiO₂ Films with PbI₂-Ethanolamine-Dimethyl Sulfoxide Solution for CsPbI₂Br₂ Perovskite Solar Cells

Xianwei Meng¹, Kailin Chi², Qian Li³, Yu Cao⁴, Gengxin Song², Bao Liu², Haibin Yang¹ and Wuyou Fu^{1,*}

¹ State Key Laboratory of Superhard Materials, Jilin University, Changchun 130012, China; xwmeng17@mails.jlu.edu.cn (X.M.); yanghb@jlu.edu.cn (H.Y.)

² School of Science, Northeast Electric Power University, Jilin 132012, China; 20182787@neepu.edu.cn (K.C.); songgengxin@neepu.edu.cn (G.S.); liubao@neepu.edu.cn (B.L.)

³ Beijing Key Lab of Cryo-Biomedical Engineering and Key Lab of Cryogenics, Technical Institute of Physics and Chemistry, Chinese Academy of Sciences, Beijing 100190, China; liqian@mail.ipc.ac.cn

⁴ School of Electrical Engineering, Northeast Electric Power University, Jilin 132012, China; ycao@neepu.edu.cn

* Correspondence: fuwy@jlu.edu.cn; Tel.: +86-431-8516-8763-801; Fax: +86-431-8516-8763-801

Received: 27 April 2020; Accepted: 14 May 2020; Published: 18 May 2020



Abstract: As one of the most frequently-used electron-transporting materials, the mesoporous titanium dioxide (m-TiO₂) film used in mesoporous structured perovskite solar cells (PSCs) can be employed for the scaffold of the perovskite film and as a pathway for electron transport, and the contact area between the perovskite and m-TiO₂ directly determines the comprehensive performance of the PSCs. Because of the substandard interface combining quality between the all-inorganic perovskite CsPbI₂Br₂ and m-TiO₂, the development of the mesoporous structured CsPbI₂Br₂ PSCs synthesized by the one-step method is severely limited. Here, we used a solution containing PbI₂, monoethanolamine (EA) and dimethyl sulfoxide (DMSO) (PED) as the interfacial modifier to enhance the contact area and modify the m-TiO₂/CsPbI₂Br₂ contact characteristics. Comparatively, the performance of the solar device based on the PED-modified m-TiO₂ layer has improved considerably, and its power conversion efficiency is up to 6.39%.

Keywords: all-inorganic perovskite; CsPbI₂Br₂; solar cell; mesoporous structure; interfacial modification

1. Introduction

Despite the advantages of simple fabrication processes, high conversion efficiency and successful techniques, the organic-inorganic perovskite solar cells (PSCs) under high humidity, high temperature and light conditions show poor stability [1–6], and since this poor stability seems unlikely to improve in the short term, scholars began researching ways to enhance the stability and efficiency of PSCs by investigating the all-inorganic hybrid PSCs [7–9]. As Cs⁺ ions have replaced organic molecules in organic-inorganic halide perovskites, the all-inorganic CsPbX₃ (X = I or Br) materials present much better ultra-violet, thermal and humid stabilities in air [10–13]. Although CsPbI₃ [14–17] and CsPbI₂Br [18–20] materials exhibit acceptable light absorption capacity and performance with a relatively narrow band gap of 1.73 eV and 1.92 eV, respectively, both are difficult to be applied in practice due to their unstable structures, which easily lead to structure or performance degradation accompanied by color changes from dark red to yellow under laboratory conditions [10,13,15,21,22]. Many important physical properties of CsPbBr₃ are known, such as high tolerance to humidity, light illumination [23] and a wide band gap of 2.30 eV [24,25]. However, extensive application in

the field of photovoltaic is limited because of the low solubility of perovskite precursors (CsBr and PbBr₂) in most organic solvents [26]. In contrast, CsPbI₂Br₂ displays the best balance features for the all-inorganic PSCs as an absorption material in terms of stability and optical properties [27–32].

In mesoporous structured perovskite solar cells, the mesoporous TiO₂ is an important electron transport material that has unique physical and chemical properties; it not only supplies the pathway for electron transport but also contacts the perovskite material to enhance the separation rate of photoinduced charges. Moreover, the interface relationships of the m-TiO₂ exert a significant influence on the performance of PSCs. Many researchers have been focused on interfacial engineering to improve the comprehensive performance of the m-TiO₂ films and have achieved many results in theory and application in the PSCs field. Briefly, the use of the interfacial modifier can effectively boost the performance and photostability of PSCs. In addition, all-inorganic CsPbI₂Br₂ PSCs could be fabricated either on planar or mesoporous structures, but the former have received more research concentration on stable power output and the latter less. To our knowledge, TiO₂ is the only mesoporous material used, and CsPbI₂Br₂ films can only be synthesized by the only two-step solution method to date [26,33,34].

Herein, we successfully fabricated the CsPbI₂Br₂ PSCs on a mesoporous structure, and the perovskite films were synthesized by a typical one-step method. The PED solution was used as the interfacial modifier to modify the m-TiO₂/CsPbI₂Br₂ interface and promote the precursor solution of CsPbI₂Br₂ further diffusing into the grain boundaries of m-TiO₂ film. Therefore, using PED on the interface can not only restrain the interface recombination to enhance the electronic transmission capability but can also promote CsPbI₂Br₂ to fill the space in m-TiO₂ film to enhance the interface combination. Compared with the standard mesoporous CsPbI₂Br₂ PSCs we synthesized, the devices with PED modification presented a better performance with a power conversion efficiency (PCE) of 6.39%.

2. Experiment

2.1. Device Fabrication

Fluorine-doped tin oxide glass substrates (FTO, 6Ω/□) were patterned with a laser etcher (OPV Tech New Energy Co., Ltd., Yingkou, China.) and cleaned sequentially by a neutral detergent, deionized water, acetone, isopropanol and ethanol by ultrasound treatment. After being dried in the air, the FTO substrate was further cleaned in an ultraviolet treatment for 15 min, and then the TiO₂ compact layer (c-TiO₂) was spin-coated on the pre-conditioned FTO substrate according to the previous report [35]. Afterwards, the mesoporous TiO₂ layer (m-TiO₂) (DysoL, 30NR, diluted with ethanol at a ratio of 1:8, w/w) was coated on the FTO/c-TiO₂ substrate by spin-coating at 5000 rpm for 30 s. After the film was dried on a hotplate at 125 °C for 5 min followed by the muffle furnace at 500 °C for 30 min, the pre-coated substrates were attained.

The following synthetic processes were carried out in a glove box under the highly purified argon environment. PED solution, which contained 2 mL DMSO (99.8%, Aladdin, Shanghai, China), 0.5 mL EA (double distillation, Aladdin, Shanghai, China) and 0.25 M PbI₂ (99.99%, Xi'an p-OLED, Xi'an, China) was heated on a hot plate at 150 °C for 30 min. While the PbI₂ dissolved completely, the PED was spin-coated on the surface of the cooled pre-coated substrates at 5000 rpm for 60 s and then heated and naturally cooled once again. For CsPbI₂Br₂, the precursor solution prepared by full dissolving 260 mg CsI and 370 mg PbBr₂ in 1 mL DMSO at 150 °C was coated on the PED film by spin-coating at the 5000 rpm for 60 s and annealed at 280 °C for 10 min subsequently. After Spiro-OMeTAD (>99%, OPV Tech New Energy Co., Ltd., Yingkou, LN, China) was spin-coated onto the CsPbI₂Br₂ films at 3000 rpm for 30 s, the samples were removed from the glove box, and a 100 nm thick Ag was deposited by thermal evaporation on the top of the Spiro-OMeTAD layer as metal electrode to complete the solar energy devices.

2.2. Device Characterizations

The crystal structures and composition of the synthesized samples were identified by X-ray diffraction (XRD, Cu K α radiation, $\lambda = 1.5418 \text{ \AA}$, Rigaku D/max2500). The morphologies and structures of the films and solar devices were observed by a scanning electron microscope (SEM, FEI MAGELLAN 400, FEI, Hillsboro, OR, USA), and an energy dispersive spectroscope (EDS) attached to the SEM column was used to analysis the element composition of the corresponding samples. X-ray photoelectron spectroscopy (XPS) spectra were measured using ESCALAB 250Xi (Thermo Scientific, Waltham, MA, UK). A UV-Vis spectrometer (UV-3600, Shimadzu, TKY, Japan) was utilized to measure the absorption spectrum at a range of 300 nm to 800 nm. The steady-state photoluminescence (PL) spectrum was collected on a Ramascope System 1000 ($\lambda_{\text{ex}} = 633 \text{ nm}$). The current-voltage (J-V) characteristics and external quantum efficiency (EQE) of the fabricated solar devices were measured by a solar cells test system (XP3000, Sanyou, Beijing, China) and an external quantum efficiency (EQE) measured system (Solar Cell Scan100, Zolix, Beijing, China), respectively.

3. Results and Discussion

3.1. X-ray Diffraction Studies and Compositional Analysis

Figure 1 shows the XRD patterns of CsPbIBr₂ films synthesized on c-TiO₂/m-TiO₂ substrates with and without PED modification. Both patterns show the main diffraction peaks at 2θ of 15.00°, 21.40°, 30.19° and 37.20° corresponding to (111), (110), (200) and (211) planes of α -phase perovskite CsPbIBr₂ [29,36,37], which confirms that both CsPbIBr₂ films synthesized by the one-step method are pure, that the PED modification has no influence on the perovskite phase or crystallinity and that no PbI₂ diffraction peak can be observed. However, as the PED solution is spin-coated on c-TiO₂/m-TiO₂ substrates without CsPbIBr₂ film, a PbI₂ characteristic peak at 12.60° can be found in the XRD pattern, and the I/Pb atomic ratio is approximate to 2:1, as confirmed from EDS spectra (Figure S1a,b respectively, Supporting Information), which means that PbI₂ presents in the m-TiO₂ film as crystals. Because of being easily soluble in DMSO, PbI₂ in the PED-modified m-TiO₂ film is redissolved in the perovskite precursor solution during the successively synthetic process of CsPbIBr₂, which explains why no PbI₂ diffraction peak is observed in Figure 1.

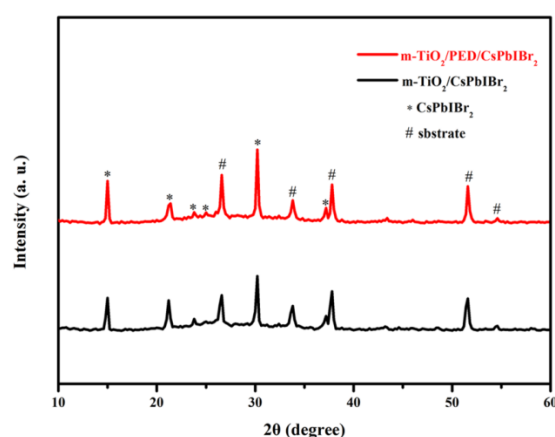


Figure 1. XRD patterns of m-TiO₂/CsPbIBr₂ films with and without PED modification.

3.2. Morphological Characterization

The influences of PED on morphologies of m-TiO₂ and CsPbIBr₂ were investigated by using SEM as shown in Figure 2. As demonstrated in Figure 2a, CsPbIBr₂ film deposited on m-TiO₂ shows a relatively porous attribute with non-uniform distribution but a smooth surface (Figure 2a). Apparently, compared with Figure 2a, the rough CsPbIBr₂ film deposited on PED-modified m-TiO₂ shown in Figure 2b is composed of almost homogeneous nanoparticles and pores that are uniformly distributed in the film. Because of the poor solubility of PbBr₂ in the perovskite precursor solution, such abundant pores in the CsPbIBr₂ film synthesized by the one-step method have seemed inevitable [26]. As illustrated in Figure 2c, pores can be clearly seen in the m-TiO₂ film, and the thickness of the CsPbIBr₂ film is about 210 nm. The cross-sectional SEM image of the PED-modified sample in Figure 2d shows that the perovskite film with a thickness of 160 nm is thinner than the pristine one and that the m-TiO₂ film is almost filled up and only a very small number of pores remain. No interface between CsPbIBr₂ and m-TiO₂ layers can be clearly distinguished. Combined with the conclusions of XRD, we can confirm that the abundant perovskite precursor solution diffuses into the m-TiO₂ film during the spin-coating process and generates CsPbIBr₂ to fill up the pores, which is conducive to the transportation and collection process for the carriers [38,39].

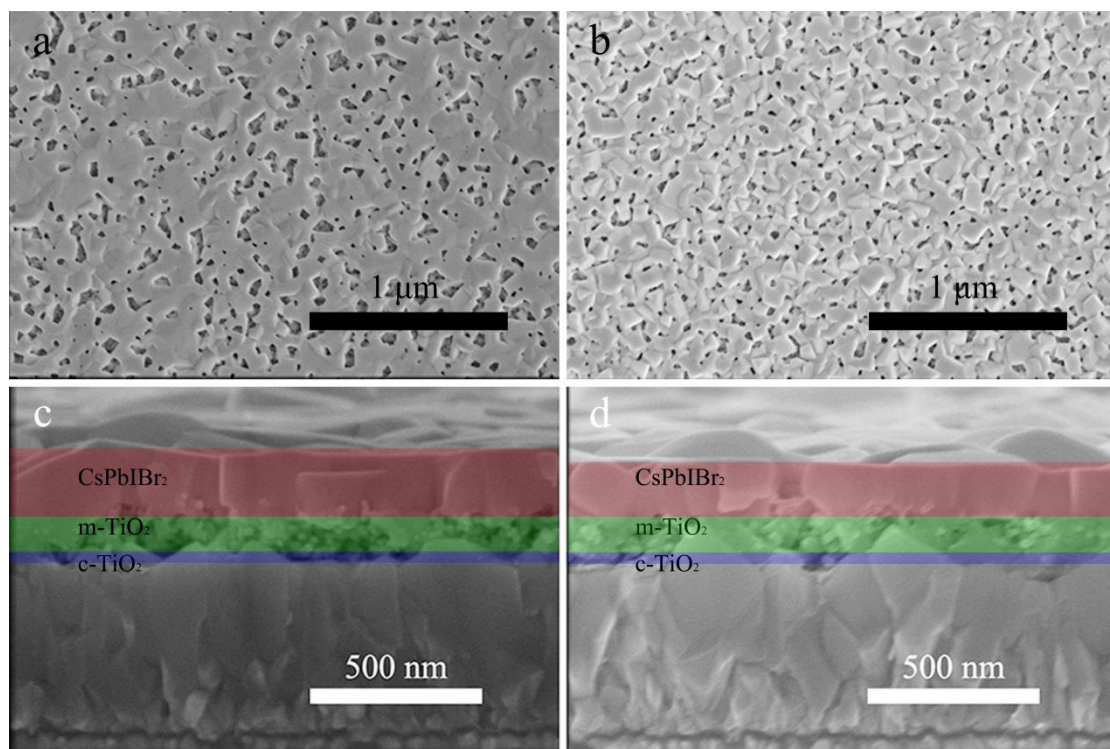


Figure 2. Top-view SEM images and cross-sectional SEM images of m-TiO₂/CsPbIBr₂ films (a,c) without and (b,d) with PED.

3.3. XPS Analysis

XPS was utilized to probe the surficial elemental composition of CsPbIBr₂ films with and without PED modification taking C 1s (284.8 eV) as the calibration. As seen from Figure 3a, obviously, the characteristic peaks of Cs, Pb, I, Br, C and O are detected, and no other element can be identified in each film. Figure 3b–e displays the XPS core spectra of corresponding Pb 4f, I 3d, Br 3d and Cs 3d, respectively. All of the binding energy peaks belonging to CsPbIBr₂ constituent elements are in accordance with previous reports [36], and no notable peak shift can be observed for each of elements. The XPS results indicate that the existence or non-existence of PED has no essential influence on the stoichiometric of the CsPbIBr₂ perovskite.

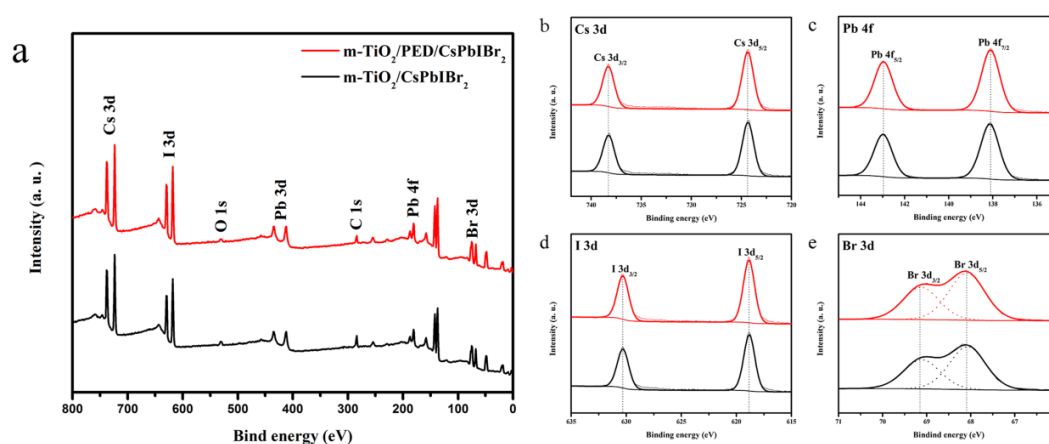


Figure 3. (a) XPS spectra and (b) Cs 3d, (c) Pb 4f, (d) I 3d and (e) Br 3d XPS core spectra of the $m\text{-TiO}_2/\text{CsPbIBr}_2$ films with and without PED modification.

3.4. Optical Properties and Photovoltaic Performances

The photophysical properties of $m\text{-TiO}_2/\text{CsPbIBr}_2$ films with and without PED modification were then studied. Figure 4a presents their absorption spectra. Both the films exhibit similar absorption profiles in the visible region. The absorbance onset for the modified sample exhibits a slight red shift from about 606 to 610 nm, and the absorption intensity increases slightly in the whole measuring range compared with the pristine sample. Correspondingly, the calculated bandgap decreases from 2.09 to 2.08 eV (Figure S2, Supporting Information), which coincides with the relevant literature [40,41]. The PL spectra are demonstrated in Figure 4b, which signifies that when the peak position of the $m\text{-TiO}_2/\text{CsPbIBr}_2$ films with PED is blue-shifted (594.9 vs 597.6 nm), the luminous intensity also distinctly decreased. Such observations suggest that the trap states of the porous TiO_2 layers that are full-filled by CsPbIBr_2 and the spontaneous radiative recombination of CsPbIBr_2 are passivated due to the interfacial modifier, PED, hence leading to the improvement of the charge separation and transfer process at the $m\text{-TiO}_2/\text{CsPbIBr}_2$ interface.

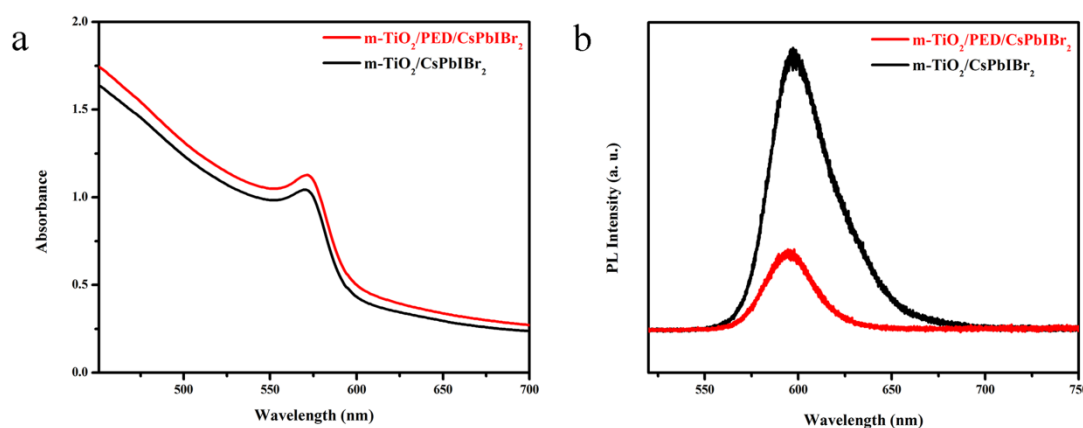


Figure 4. (a) UV-vis absorbance spectra and (b) photoluminescence (PL) spectra of the $m\text{-TiO}_2/\text{CsPbIBr}_2$ films with and without PED modification.

The PSCs we successfully synthesized were based on the simple architecture of $c\text{-TiO}_2/m\text{-TiO}_2/\text{PED}$ (or not)/ $\text{CsPbIBr}_2/\text{Spiro-OMeTAD}/\text{Ag}$, and the cross-section of the complete modified device is given in Figure 5a. Figure 5b provides the reverse- and forward-scanned J - V curves of two representative devices measured under simulated AM 1.5G illumination. The hysteresis index (HI) was applied

to assess the hysteresis effect of the devices, which can be well defined according to the following equation [42]:

$$HI = \frac{PCE_{reverse} - PCE_{forward}}{PCE_{reverse}}$$

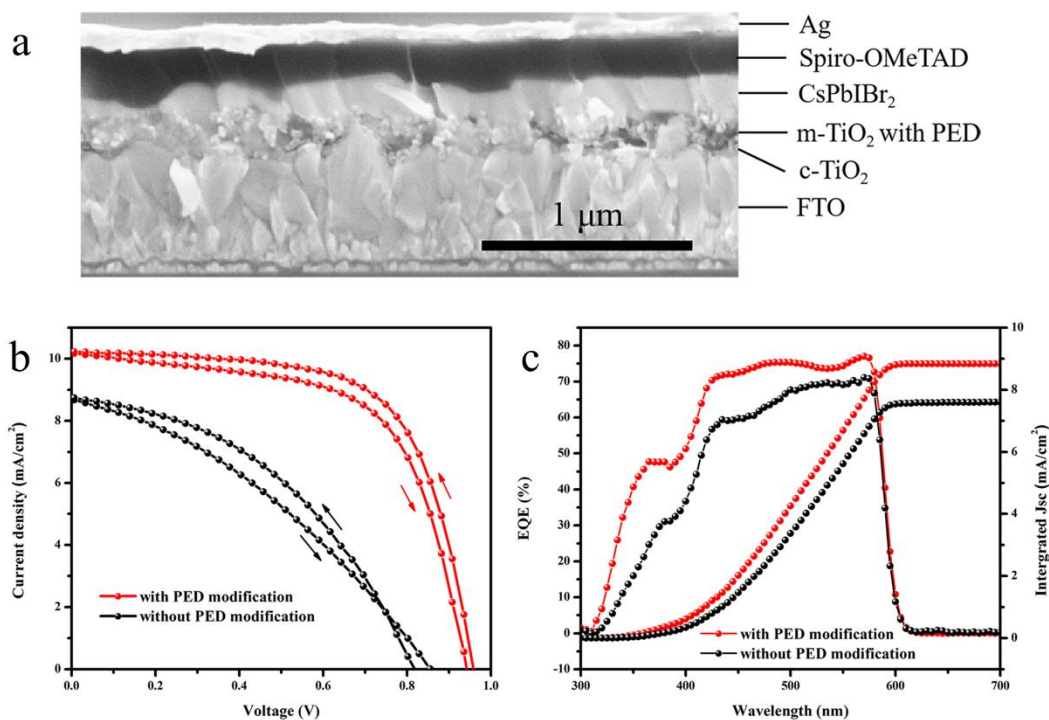


Figure 5. (a) Cross-sectional SEM image of the modified CsPbIBr₂ devices. (b) *J*-*V* curves and (c) EQE spectra and the integrated product of the EQE curve of the corresponding devices.

Compared with the pristine device, the m-TiO₂/PED device shows an expected slighter hysteresis behavior (a decrease from 13.8% to 7.2%), and all photovoltaic parameters including short circuit current density (J_{SC}), open circuit voltage (V_{OC}), fill factor (FF) and PCE are enhanced evidently. As listed in Table 1, the PED modification of m-TiO₂ has significantly increased the J_{SC} from 8.69–8.74 mA·cm⁻² to 10.22–10.28 mA·cm⁻², V_{OC} from 0.82–0.86 V to 0.94–0.96 V and FF from 0.35–0.43 to 0.62–0.65, leading to an efficiency improvement of more than 110% from 2.62–3.04% to 5.93–6.39%. The EQE spectra and the corresponding integral current densities are provided in Figure 5c. Both EQE spectra present the same onsets at the wavelength of about 600 nm, which are roughly consistent with the results of absorption spectrum. A significant enhancement of EQE values is observed for the m-TiO₂/PED device in the light absorption wavelength range of 300–575 nm, which is consistent with the increment in J_{SC} . Meanwhile, the integrated current densities from EQE are close to the results of J_{SC} , while the discrepancy mainly originates from the spectral mismatch between the solar simulator and EQE measurement system.

Table 1. Photovoltaic parameters of the CsPbIBr₂ devices with and without PED modification.

Substrate	Scan	J_{sc} (mA·cm ⁻²)	V_{oc} (V)	FF	PCE (%)
Without PED	forward	8.69	0.86	0.35	2.62
	reverse	8.74	0.82	0.43	3.04
With PED	forward	10.28	0.94	0.62	5.93
	reverse	10.22	0.96	0.65	6.39

3.5. Possible Mechanism

The enhancement of power conversion efficiency of the CsPbIBr₂ device was mainly ascribed to the PED solution, which contained proper EA and PbI₂. The –OH group of EA within the PED solution would interact with PbI₂ colloid (such as PbI₃[−] and PbI₄^{2−}) to form stable chemical bonding –OH–Pb [43]. As shown in Figure 6, while PED was spin-coated on m-TiO₂, the unreacted PbI₂ was forced to penetrate into the TiO₂ mesoporous film by –OH group [44]. While the CsPbIBr₂ precursor solution was coated on the m-TiO₂/PED substrate, PbI₂ in the mesoporous film provided the paths for the precursor solution diffusing into the pores while –OH–Pb coordinated to the TiO₂ surface to improve the interface contact with CsPbIBr₂ [43]. Therefore, the holes and chink were packed and closed by CsPbIBr₂ in the annealing process, leading to the decreasing thickness of the CsPbIBr₂ film on the m-TiO₂/PED substrate. It should be noted that the surface color of m-TiO₂/PED gradually converted from light yellow into colorless during the spin-coated process of the CsPbIBr₂ precursor solution. This phenomenon was caused by the fact that PbI₂ deposited in porous TiO₂ was redissolved in the perovskite precursor solution and participated in the CsPbIBr₂ growth and film-forming processes, leaving native defects due to nonstoichiometry [45,46]. That explains why the diffraction peak of PbI₂ could not be found in the XRD pattern and why the morphology of the CsPbIBr₂ surface also changed for the m-TiO₂/PED/ CsPbIBr₂ film. Furthermore, the improvement of the optical properties of the modified sample based on UV-Vis spectra and EQE spectra was mainly attributable to the CsPbIBr₂ filling behavior and the stoichiometric change in the mesoporous film. The pores filled by perovskite in m-TiO₂ could effectively increase the contact area between TiO₂ nanoparticles and CsPbIBr₂. The –OH–Pb group was advantageous for enhancing the interface contact, reducing trap states of the perovskite film, improving the electron extraction and charging transport rates [47,48], as well as restraining the recombination of charge carriers at the interface to help decrease the hysteresis of CsPbIBr₂ device, as proved by the PL and J-V measurements.

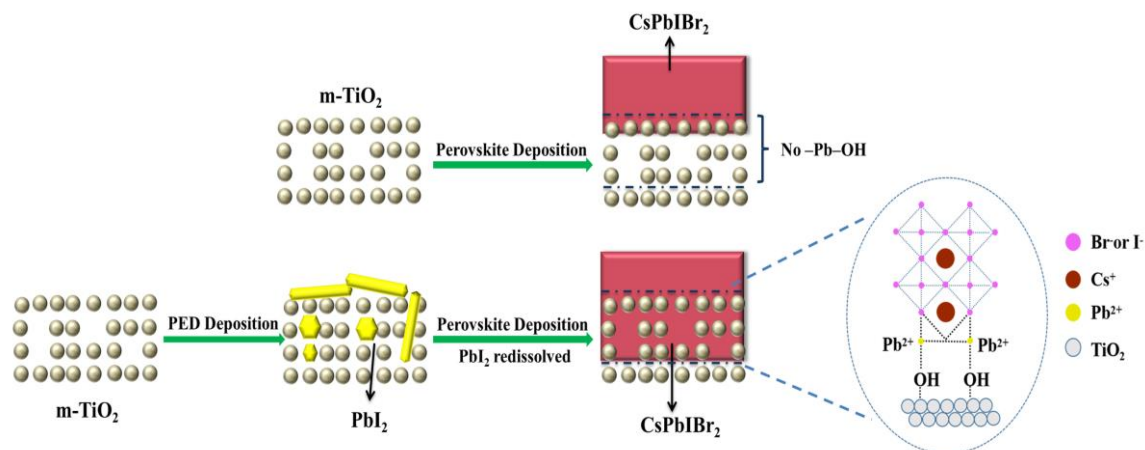


Figure 6. Schematic diagram illustrating the deposition of CsPbIBr₂ perovskite on m-TiO₂. The upper row shows the normal procedure to synthesize CsPbIBr₂ film on m-TiO₂. The lower row is the CsPbIBr₂ deposition on the PED/m-TiO₂ substrate.

4. Conclusions

In this work, we have successfully utilized PED solution as the interfacial modifier to modify the c-TiO₂/m-TiO₂ substrates, and the influence of PED on the CsPbIBr₂ PSCs, which were synthesized by the one-step method on the mesoporous structure, was studied. By using a PED solution, CsPbIBr₂ efficiently fills the pores of the m-TiO₂ to enhance the m-TiO₂/CsPbIBr₂ interfacial contact area and to optimize the contact characteristics due to the combination of PbI₂ with EA. The PCE of the modified solar device has been significantly promoted from about 3.0% to over 6.3%, with an enhancement of 110% compared with the pristine one. The –OH–Pb group in PED is the main reason for the

improvement of optical properties and the optimization of comprehensive performance for the modified device.

Supplementary Materials: The following are available online at <http://www.mdpi.com/2079-4991/10/5/962/s1>, Figure S1: (a) XRD pattern and (b) EDS spectra of the m-TiO₂/PED film; Figure S2: $(\alpha h\nu)^2$ vs. $h\nu$ plots of the m-TiO₂/CsPbI₃Br₂ with and without PED modification.

Author Contributions: W.F. and H.Y. conceived the idea; X.M., K.C. and Q.L. performed research, analyzed data and wrote the paper; Y.C., G.S. and B.L. contributed to refining the ideas and finalizing the paper. All authors have read and agreed to the published version of the manuscript.

Funding: This work was financially supported by the National Natural Science Foundation of China (NO.51272086).

Conflicts of Interest: The authors declare no conflict of interest.

References

1. Conings, B.; Drijkoningen, J.; Gauquelin, N.; Babayigit, A.; D'Haen, J.; D'Olieslaeger, L.; Ethirajan, A.; Verbeeck, J.; Manca, J.; Mosconi, E.; et al. Intrinsic thermal instability of methylammonium lead trihalide perovskite. *Adv. Energy Mater.* **2015**, *5*, 1500477. [[CrossRef](#)]
2. Han, Y.; Meyer, S.; Dkhissi, Y.; Weber, K.; Pringle, J.M.; Bach, U.; Spiccia, L.; Cheng, Y.B. Degradation observations of encapsulated planar CH₃NH₃PbI₃ perovskite solar cells at high temperatures and humidity. *J. Mater. Chem. A* **2015**, *3*, 8139–8147. [[CrossRef](#)]
3. Park, Y.H.; Jeong, I.; Bae, S.; Son, H.J.; Lee, P.; Lee, J.; Lee, C.H.; Ko, M.J. Inorganic rubidium cation as an enhancer for photovoltaic performance and moisture stability of HC(NH₂)₂PbI₃ perovskite solar cells. *Adv. Funct. Mater.* **2017**, *27*, 1605988. [[CrossRef](#)]
4. Akbulatov, A.F.; Luchkin, S.Y.; Frolova, L.A.; Dremova, N.N.; Gerasimov, K.L.; Zhidkov, I.S.; Anokhin, D.V.; Kurmaev, E.Z.; Stevenson, K.J.; Troshin, P.A. Probing the intrinsic thermal and photochemical stability of hybrid and inorganic lead halide perovskites. *J. Phys. Chem. Lett.* **2017**, *8*, 1211–1218. [[CrossRef](#)]
5. Zhou, W.; Zhao, Y.C.; Zhou, X.; Fu, R.; Li, Q.; Zhao, Y.; Liu, K.H.; Yu, D.P.; Zhao, Q. Light-independent ionic transport in inorganic perovskite and ultrastable Cs-based perovskite solar cells. *J. Phys. Chem. Lett.* **2017**, *8*, 4124–4128. [[CrossRef](#)]
6. Sutter-Fella, C.M.; Ngo, Q.P.; Cefarin, N.; Gardner, K.L.; Tamura, N.; Stan, C.V.; Drisdell, W.S.; Javey, A.; Toma, F.M.; Sharp, I.D. Cation-dependent light-induced halide demixing in hybrid organic-inorganic perovskites. *Nano Lett.* **2018**, *18*, 3473–3480. [[CrossRef](#)]
7. Kojima, A.; Teshima, K.; Shirai, Y.; Miyasaka, T. Organometal halide perovskites as visible-light sensitizers for photovoltaic cells. *J. Am. Chem. Soc.* **2009**, *131*, 6050–6051. [[CrossRef](#)]
8. Jeon, N.J.; Na, H.; Jung, E.H.; Yang, T.-Y.; Lee, Y.G.; Kim, G.; Shin, H.-W.; Seok, S.I.; Lee, J.; Seo, J. A fluorene-terminated hole-transporting material for highly efficient and stable perovskite solar cells. *Nat. Energy* **2018**, *3*, 682–688. [[CrossRef](#)]
9. Christians, J.A.; Schulz, P.; Tinkham, J.S.; Schloemer, T.H.; Harvey, S.P.; Tremolet de Villers, B.J.; Sellinger, A.; Berry, J.J.; Luther, J.M. Tailored interfaces of unencapsulated perovskite solar cells for >1,000 hour operational stability. *Nat. Energy* **2018**, *3*, 68–74. [[CrossRef](#)]
10. Chen, H.; Xiang, S.; Li, W.; Liu, H.; Zhu, L.; Yang, S. Inorganic perovskite solar cells: A rapidly growing field. *Solar RRL* **2018**, *2*, 1700188. [[CrossRef](#)]
11. Bian, H.; Bai, D.L.; Jin, Z.W.; Wang, K.; Liang, L.; Wang, H.R.; Zhang, J.R.; Wang, Q.; (Frank)Liu, S.Z. Graded bandgap CsPbI_{2+x}Br_{1-x} perovskite solar cells with a stabilized efficiency of 14.4%. *Joule* **2018**, *2*, 1500–1510. [[CrossRef](#)]
12. Dastidar, S.; Li, S.; Smolin, S.Y.; Baxter, J.B.; Fafarman, A.T. Slow electron-hole recombination in lead iodide perovskites does not require a molecular dipole. *ACS Energy Lett.* **2017**, *2*, 2239–2244. [[CrossRef](#)]
13. Liang, J.; Liu, J.; Jin, Z. All-inorganic halide perovskites for optoelectronics: Progress and prospects. *Solar RRL* **2017**, *1*, 1700086. [[CrossRef](#)]
14. Wang, Q.; Zheng, X.; Deng, Y.; Zhao, J.; Chen, Z.; Huang, J. Stabilizing the α -Phase of CsPbI₃ perovskite by sulfobetaine zwitterions in one-step spin-coating films. *Joule* **2017**, *1*, 371–382. [[CrossRef](#)]
15. Eperon, G.E.; Paterno, G.M.; Sutton, R.J.; Zampetti, A.; Haghighirad, A.A.; Cacialli, F.; Snaith, H.J. Inorganic caesium lead iodide perovskite solar cells. *J. Mater. Chem. A* **2015**, *3*, 19688–19695. [[CrossRef](#)]

16. Hu, Y.; Bai, F.; Liu, X.; Ji, Q.; Miao, X.; Qiu, T.; Zhang, S. Bismuth incorporation stabilized α -CsPbI₃ for fully inorganic perovskite solar cells. *ACS Energy Lett.* **2017**, *2*, 2219–2227. [[CrossRef](#)]
17. Chen, C.Y.; Lin, H.Y.; Chiang, K.M.; Tsai, W.L.; Huang, Y.C.; Tsao, C.S.; Lin, H.-W. All-vacuum-deposited stoichiometrically balanced inorganic cesium lead halide perovskite solar cells with stabilized efficiency exceeding 11%. *Adv. Mater.* **2017**, *29*, 1605290. [[CrossRef](#)]
18. Xiang, W.; Wang, Z.; Kubicki, D.J.; Tress, W.; Luo, J.; Prochowicz, D.; Akin, S.; Emsley, L.; Zhou, J.; Dietler, G.; et al. Hagfeldt, Europium-doped CsPbI₂Br for stable and highly efficient inorganic perovskite solar cells. *Joule* **2019**, *3*, 205–214. [[CrossRef](#)]
19. Shen, E.; Chen, J.; Tian, Y.; Luo, Y.; Shen, Y.; Sun, Q.; Jin, T.; Shi, G.; Li, Y.; Tang, J. Interfacial energy level tuning for efficient and thermostable CsPbI₂Br perovskite solar cells. *Adv. Sci.* **2020**, *7*, 1901952. [[CrossRef](#)]
20. Rao, H.; Ye, S.; Gu, F.; Zhao, Z.; Liu, Z.; Bian, Z.; Huang, C. Morphology controlling of all-inorganic perovskite at low temperature for efficient rigid and flexible solar cells. *Adv. Energy Mater.* **2018**, *8*, 1800758. [[CrossRef](#)]
21. Wang, Y.; Zhang, T.; Kan, M.; Zhao, Y. Bifunctional stabilization of all-inorganic α -CsPbI₃ perovskite for 17% efficiency photovoltaics. *J. Am. Chem. Soc.* **2018**, *140*, 12345–12348. [[CrossRef](#)] [[PubMed](#)]
22. Guo, Z.; Zhao, S.; Liu, A.; Kamata, Y.; Teo, S.; Yang, S.; Xu, Z.; Hayase, S.; Ma, T. Niobium, Incorporation into CsPbI₂Br for stable and efficient all-inorganic perovskite solar cells. *ACS Appl. Mater. Interfaces* **2019**, *11*, 19994–20003. [[CrossRef](#)] [[PubMed](#)]
23. Zhang, X.S.; Jin, Z.W.; Zhang, J.R.; Bai, D.L.; Bian, H.; Wang, K.; Sun, J.; Wang, Q.; Frank Liu, S.Z. All-ambient processed binary CsPbBr₃-CsPb₂Br₅ perovskites with synergistic enhancement for high-efficiency Cs-Pb-Br-based solar cells. *ACS Appl. Mater. Interfaces.* **2018**, *10*, 7145–7154. [[CrossRef](#)] [[PubMed](#)]
24. Liang, J.; Wang, C.; Wang, Y.; Xu, Z.; Lu, Z.; Ma, Y.; Zhu, H.; Hu, Y.; Xiao, C.; Yi, X.; et al. All-inorganic perovskite solar cells. *J. Am. Chem. Soc.* **2016**, *138*, 15829–15832. [[CrossRef](#)]
25. Duan, J.; Zhao, Y.; He, B.; Tang, Q. High-purity inorganic perovskite films for solar cells with 9.72% efficiency. *Angew. Chem.* **2018**, *57*, 3787–3791. [[CrossRef](#)]
26. Lau, C.F.J.; Deng, X.F.; Ma, Q.S.; Zheng, J.H.; Yun, J.S.; Green, M.A.; Huang, S.J.; Ho-Baillie, A.W.Y. CsPbIBr₂ perovskite solar cell by spray-assisted deposition. *ACS Energy Lett.* **2016**, *1*, 573–577. [[CrossRef](#)]
27. Ma, Q.; Huang, S.; Wen, X.; Green, M.A.; Ho-Baillie, A.W.Y. Hole transport layer Free inorganic CsPbIBr₂ perovskite solar cell by dual source thermal evaporation. *Adv. Energy Mater.* **2016**, *6*, 1502202. [[CrossRef](#)]
28. Lin, J.; Lai, M.; Dou, L.; Kley, C.S.; Chen, H.; Peng, F.; Sun, J.; Lu, D.; Hawks, S.A.; Xie, C.; et al. Thermochromic halide perovskite solar cells. *Nat. Mater.* **2018**, *17*, 261–267. [[CrossRef](#)]
29. Zhang, Q.; Zhu, W.; Chen, D.; Zhang, Z.; Lin, Z.; Chang, J.; Zhang, J.; Zhang, C.; Hao, Y. Light processing enables efficient carbon-based, all-inorganic planar CsPbIBr₂ solar cells with high photovoltages. *ACS Appl. Mater. Interfaces* **2019**, *11*, 2997–3005. [[CrossRef](#)]
30. Sutton, R.J.; Eperon, G.E.; Miranda, L.; Parrott, E.S.; Kamino, B.A.; Patel, J.B.; Horantner, M.T.; Johnston, M.B.; Haghighirad, A.A.; Moore, D.T. Bandgap-tunable cesium lead halide perovskites with high thermal stability for efficient solar cells. *Adv. Energy Mater.* **2016**, *6*, 1502458. [[CrossRef](#)]
31. Guo, Y.; Yin, X.; Liu, J.; Wen, S.; Wu, Y.; Que, W. Inorganic CsPbIBr₂-based perovskite solar cells: Fabrication technique modification and efficiency improvement. *Sol. RRL* **2019**, *3*, 1900135. [[CrossRef](#)]
32. Liu, C.; Li, W.; Chen, J.; Fan, J.; Mai, Y.; Schropp, R.E. Ultra-thin MoO_x as cathode buffer layer for the improvement of all-inorganic CsPbIBr₂ perovskite solar cells. *Nano Energy* **2017**, *41*, 75–83. [[CrossRef](#)]
33. Liang, J.; Liu, Z.H.; Qiu, L.B.; Hawash, Z.; Meng, L.Q.; Wu, Z.F.; Jiang, Y.; Ono, L.K.; Qi, Y.B. Enhancing optical, electronic, crystalline, and morphological properties of cesium lead halide by Mn substitution for high-stability all-inorganic perovskite solar cells with carbon electrodes. *Adv. Energy Mater.* **2018**, *8*, 1800504. [[CrossRef](#)]
34. Liang, J.; Zhao, P.Y.; Wang, C.X.; Wang, Y.R.; Hu, Y.; Zhu, G.Y.; Ma, L.B.; Liu, J.; Jin, Z. CsPb_{0.9}Sn_{0.1}IBr₂ based all-Inorganic perovskite solar cells with exceptional efficiency and stability. *J. Am. Chem. Soc.* **2017**, *139*, 14009–14012. [[CrossRef](#)]
35. Kim, S.; Chung, T.; Bae, S.; Lee, S.-W.; Lee, K.D.; Kim, H.; Lee, S.; Kang, Y.; Lee, H.S.; Kim, D. Improved performance and thermal stability of perovskite solar cells prepared via a modified sequential deposition process. *Org. Electron.* **2017**, *41*, 266–273. [[CrossRef](#)]
36. Zhu, W.D.; Zhang, Q.N.; Chen, D.Z.; Zhang, Z.Y.; Lin, Z.H.; Chang, J.J.; Zhang, J.C.; Zhang, C.F.; Hao, Y. Intermolecular exchange boosts efficiency of air-stable, carbon-based all-Inorganic planar CsPbIBr₂ perovskite solar cells to Over 9%. *Adv. Energy Mater.* **2018**, *8*, 1802080. [[CrossRef](#)]

37. Lu, J.J.; Chen, S.C.; Zheng, Q.D. Defect Passivation of CsPbIBr₂ perovskites for high-performance solar cells with large open-circuit voltage of 1.28 V. *ACS Appl. Energy Mater.* **2018**, *1*, 5872–5878. [[CrossRef](#)]
38. Hwang, T.; Lee, S.; Kim, J.; Kim, J.; Kim, C.; Shin, B.; Park, B. Tailoring the mesoscopic TiO₂ layer: Concomitant parameters for enabling high-performance perovskite solar cells. *Nanoscale Res. Lett.* **2017**, *12*, 57. [[CrossRef](#)]
39. Divitini, G.; Cacovich, S.; Matteocci, F.; Cinà, L.; Carlo, A.D.; Ducati, C. In situ observation of heat-induced degradation of perovskite solar cells. *Nat. Energy* **2016**, *1*, 15012. [[CrossRef](#)]
40. Yang, B.; Wang, M.; Hu, X.F.; Zhou, T.W.; Zang, Z.G. Highly efficient semitransparent CsPbIBr₂ perovskite solar cells via low temperature processed In₂S₃ as electron-transport-layer. *Nano Energy* **2019**, *57*, 718–727. [[CrossRef](#)]
41. Guo, Y.X.; Yin, X.T.; Liu, J.; Que, W.X. Highly efficient CsPbIBr₂ perovskite solar cells with efficiency over 9.8% fabricated using a preheating-assisted spin-coating method. *J. Mater. Chem. A* **2019**, *7*, 19008–19016. [[CrossRef](#)]
42. Ahn, N.; Jeon, I.; Yoon, J.; Kauppinen, E.; Matsuo, Y.; Maruyama, S.; Choi, M. Carbon-sandwiched perovskite solar cell. *J. Mater. Chem. A* **2018**, *6*, 1382–1389. [[CrossRef](#)]
43. Bai, Y.; Chen, H.; Xiao, S.; Xue, Q.; Zhang, T.; Zhu, Z.; Li, Q.; Hu, C.; Yang, Y.; Hu, Z.C.; et al. Effects of a molecular monolayer modification of NiO nanocrystal layer surfaces on perovskite crystallization and interface contact toward faster hole extraction and higher photovoltaic performance. *Adv. Funct. Mater.* **2016**, *26*, 2950–2958. [[CrossRef](#)]
44. Peng, Q.M.; Guo, J.X.; Zhang, Q.R.; Xiang, J.Y.; Liu, B.Z.; Zhou, A.G.; Liu, R.P.; Tian, Y.J. Unique lead adsorption behavior of activated hydroxyl group in two-dimensional titanium carbide. *J. Am. Chem. Soc.* **2014**, *136*, 4113–4116. [[CrossRef](#)]
45. Shi, B.; Yao, X.; Hou, F.H.; Guo, S.; Li, Y.C.; Wei, C.C.; Ding, Y.; Li, Y.L.; Zhao, Y.; Zhang, X.D. Unraveling the passivation process of PbI₂ to enhance the efficiency of planar perovskite solar cells. *J. Phys. Chem. C.* **2018**, *122*, 21269–21276. [[CrossRef](#)]
46. Yu, H.; Lu, H.P.; Xie, F.Y.; Zhou, S.; Zhao, N. Native defect-induced hysteresis behavior in organolead iodide perovskite solar cells. *Adv. Funct. Mater.* **2016**, *26*, 1411–1419. [[CrossRef](#)]
47. Ahn, N.; Kwak, K.; Jang, M.S.; Yoon, H.; Lee, B.Y.; Lee, J.K.; Pikhitsa, P.V.; Byun, J.; Choi, M. Trapped charge-driven degradation of perovskite solar cells. *Nat. Commun.* **2016**, *7*, 13422. [[CrossRef](#)]
48. Lin, H.S.; Jen, I.I.; Chen, Y.Q.; Yang, X.Y.; Nakagawa, T.; Maruyama, S.; Manzhos, S.; Matsuo, Y. Highly selective and scalable fullerene-cation-mediated synthesis accessing cyclo [60] fullerenes with five-membered carbon ring and their application to perovskite solar cells. *Chem. Mater.* **2019**, *31*, 8432–8439. [[CrossRef](#)]



© 2020 by the authors. Licensee MDPI, Basel, Switzerland. This article is an open access article distributed under the terms and conditions of the Creative Commons Attribution (CC BY) license (<http://creativecommons.org/licenses/by/4.0/>).